Solvent and A-site cation control preferred crystallographic orientation in bromine-based perovskite thin films

Juanita Hidalgo [1], Yu An [1], Dariia Yehorova [2], Ruipeng Li [3], Joachim Breternitz [4], Carlo A.R. Perini [1], Armin Hoell [4], Pablo P. Boix [5], Susan Schorr [4,6], Joshua S. Kretchmer [2]*, Juan-Pablo Correa-Baena [1]*

[1] School of Materials Science and Engineering, Georgia Institute of Technology, Atlanta, Georgia 30332, United States.

[2] School of Chemistry and Biochemistry, Georgia Institute of Technology, Atlanta, Georgia 30332, United States.

[3] National Synchrotron Light Source II, Brookhaven National Lab, Upton, New York, 11973, United States.

[4] Department of Structure and Dynamics of Energy Materials, Helmholtz Zentrum Berlin für Materialien und Energie, Hahn-Meitner-Platz 1, 14109, Berlin, Germany.

[5] Institut de Ciència dels Materials, Universidad de València, C/J. Beltran 2, Paterna, 46980 Valencia, Spain.

[6] Freie Universitaet Berlin, Institute of Geological Sciences, Malteser Str. 74-200, 12249 Berlin, Germany.

Corresponding Authors: JSK jkretchmer@gatech.edu, and JPCB jpcorrea@gatech.edu

ORCID:
Juanita Hidalgo 0000-0002-5832-3262
Yu An 0000-0002-1382-5293
Dariia Yehorova 0000-0002-4091-4945
Ruipeng Li
Joachim Breternitz
Carlo A.R Perini 0000-0001-7582-2234
Armin Hoell 0000-0002-7080-8393
Pablo P. Boix 0000-0001-9518-7549
Susan Schorr 0000-0002-6687-614X
Joshua S. Kretchmer 0000-0003-3468-0481
Juan-Pablo Correa-Baena 0000-0002-3860-114

Table of Contents

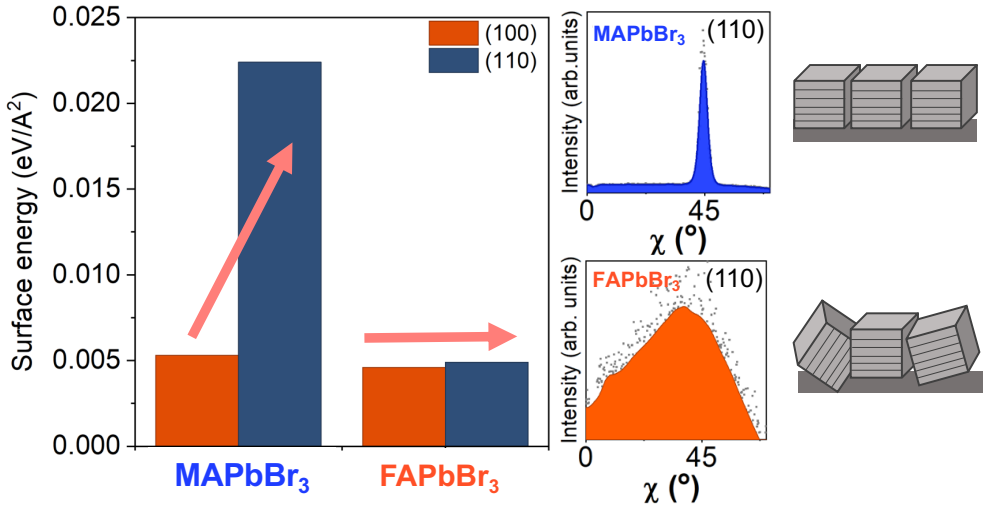

Abstract

Preferred crystallographic orientation in polycrystalline films is desirable for efficient charge carrier transport in metal halide perovskites and semiconductors, more generally. However, the mechanisms that determine the preferred orientation of halide perovskites are still not well understood. In this work, we investigate crystallographic orientation in lead bromide perovskites. We show that both the solvent of the precursor solution and organic A-site cation strongly affect the preferred orientation of the deposited perovskite thin films. In the former, we show that dimethylsulfoxide dominates the early stages of crystallization by preventing colloidal particle interactions and, thus, the preferred orientation of the deposited polycrystalline thin films. Additionally, the methylammonium A-site cation induces a higher degree of preferred orientation than the formamidinium counterpart. We use density functional theory to show that the surface energy of the (100) plane facets is lower than the (110) planes in methylammonium-based perovskites. In contrast, the surface energy of the (100) and (110) facets are similar for formamidinium materials due to the ability of the organic cations to reorient with respect to the bulk geometry for the (110) plane facets. This relative degeneracy for the surfaces involving formamidinium helps explain the large orientational disorder in formamidinium compared to the

higher degree of preferred orientation of the (100) plane parallel to the substrate for methylammonium. Finally, we show that different A-site cations, with differences in crystallographic orientation, do not significantly impact ion diffusion in bromine-based perovskite solar cells, but do impact ion density, increasing hysteresis. Our work shows that a high degree of orientation stems from an interplay between solvent and organic A-site cation and that it plays a crucial role in the electronic properties and ionic migration in solar cells.

1. Introduction

Preferred crystallographic orientation in polycrystalline films is highly desired for better charge carrier transport in organic-inorganic lead halide perovskite solar cells. For example, oriented crystallographic domains have been shown to enhance charge carrier transport [1] and suppress ionic migration [2] in lead halide perovskite films. Therefore, manipulating the degree of crystallographic orientation presents an important design principle [3–5]. Furthermore, organic-inorganic lead bromide perovskites, in comparison to the more common lead iodide perovskites, have also shown potential for multijunction perovskite solar cells because of their wide bandgap and phase stability [6–8]. Beyond solar cells, lead bromide perovskites have been used for light-emitting devices [9] and photodetectors [10,11]. For these reasons, understanding the structure-property relationships of bromine-based perovskites is fundamental to designing better optoelectronic devices. In particular, the underlying mechanisms that dominate crystallographic orientation in lead bromide perovskites are underexplored.

Solvent engineering has been used to control the crystallization kinetics and different properties of perovskite polycrystalline thin films [11–16]. The highest power conversion efficiency in perovskite solar cells has been through solution processing utilizing a precursor solution of a mixture of N,N-dimethylformamide (DMF), and dimethyl sulfoxide (DMSO) [12]. Differences in coordination between the solvent, DMF or DMSO, with the perovskite precursors salts (e.g.,

MABr, FABr, $PbBr_2$) have led to variations in the crystallization process, affecting the film morphology and crystallographic orientation [16–18]. Solvent coordination influences the formation of colloidal particles in solution, which has an important effect on the overall crystallization process and perovskite thin film morphology [19–21]. For example, adding an optimum amount of DMSO slows down crystallization and helps control crystallinity in halide perovskites [12,14,22,23]. Instead, DMF coordinates weakly, leading to a faster and poorly-controlled crystallization [14,23]. The colloids in the precursor solution may lead to agglomerations, interactions within colloidal particles, and intermediate solvent-perovskite phases, all of which have an effect on the crystallized film [19,20,24]. In particular, iodide-based lead perovskites form numerous types of iodo-plumbate structures in solution and other solvent-perovskite phases both in DMF and DMSO [15,18,25]. Ray et al. studied and observed important differences in the precursor solution colloids leading to different final structures in Cs-Pb-Br complexes [21].

In lead halide perovskites $APbBr_3$, A can be the inorganic Cs atom or the organic methylammonium (MA) or formamidinium (FA) molecule [1,3–5,26]. The A-site cation has also been shown to play a role in the crystallization behavior of halide perovskite thin films. For example, Petrov et al. showed that FA and MA led to different solvent-halo-plumbate complexes. For the Br-based compositions, they showed that the combination of MABr and $PbBr_2$ in DMF or DMSO did not form any solvent intermediate phase as it converted directly into $MAPbBr_3$ perovskite [18]. However, in the case of FA, combining FABr and $PbBr_2$ in DMSO, a solvent intermediate phase $(FA)_2PbBr_4$-DMSO was formed [11,18]. This suggests that the A-site cation has a very strong influence on the crystallization of thin films. An et al. studied the Cs-FA iodide-bromide compositional space from a pure DMSO precursor solution, showing that the film became more oriented when Cs and Br were added [27]. In agreement with An, Steele et al. [26] studied the

crystallographic orientation of all-inorganic lead iodide perovskites, where they found that incorporating Br into $CsPbI_3$ reduced the orthorhombic lattice distortion and led to energetically favored crystallographic orientations. Zheng et al. [3] manipulated the crystallographic orientation of lead halide perovskites by incorporating alkali metal cations such as Cs and Rb into the A-site. These different studies have shown that both solvent differences and composition will influence the orientation. Further, separating the solvent and composition (A-site cation) effects are important to understand the dominating factors that lead to a high degree of orientation for an optimal material design.

Herein, we investigate the role of the solvent and, importantly, of the organic A-site cation in controlling crystallographic orientation in lead bromide perovskites. To understand polycrystalline film orientation, we start from the early stages of crystallization by analyzing the precursor solutions through small-angle X-ray scattering (SAXS). We study the two organic cations MA and FA, both in DMF and DMSO, to unravel the A-site cation effect in orientation. Crystallographic film orientation is analyzed by grazing-incidence wide-angle X-ray scattering (GIWAXS). We observe an interplay between solvent and A-site cation that dominates the crystallographic orientation in lead bromide perovskites. We observe that DMSO creates a highly oriented film, compared to a more random orientation, when using DMF. For the A-site cation, regardless of the solvent, $MAPbBr_3$ shows a higher degree of orientation compared to $FAPbBr_3$. By calculating the surface energy of the (100) and (110) plane facets, we see that $MAPbBr_3$ is thermodynamically favored to have the (100) planes oriented parallel to the surface; in comparison, $FAPbBr_3$ exhibits a near degeneracy between the (100) and (110) facets, leading to a lower degree of preferred orientation. In addition, we show that the A-site cation, given differences in preferred orientation, does not affect ionic diffusion but does change the ionic density as function of a bias, shown in

impedance spectroscopy. The latter causes hysteresis behavior in solar cells. Our findings provide valuable guidelines for designing lead bromide perovskites with an optimum degree of preferred crystallographic orientation for optimal performance.

2. Methodology

Experimental

Perovskite precursor solution. We prepared a 1.24M A-$PbBr_3$ perovskite precursor solution for A: MA or FA. The stoichiometry of the solution was a 5% molar excess of the organic cation. The solvent used was DMF, or DMSO, or a volume ratio of 4:1 DMF to DMSO. The solution was stirred for one hour before deposition in a nitrogen glovebox. The solution was kept in nitrogen before any characterization measurement, at room temperature.

Perovskite thin film deposition. The lead bromide perovskite precursor solution was spin-coated to an indium-doped tin oxide (ITO)/glass or glass substrate in a two-step program: first at 1000 revolutions per minute (rpm) for 10 s (acceleration of 1000 rpm/s) and then at 6000 rpm for 20 s (acceleration of 2000 rpm/s). During the spin-coating process, 250 µL of chlorobenzene (CB) was added. For the perovskites in DMF, the CB was added at the start of the second speed step, whereas for perovskites in DMSO, the CB was added 5 seconds before the end of the second step. After deposition of the perovskite solution, the substrates were annealed at 100°C for 30 min in a nitrogen glove box.

Theoretical calculations

The surface energies, γ, of $FAPbBr_3$ and $MAPbBr_3$ with different surface orientations were calculated using the following definition:

$$\gamma = \frac{(E_{slab} - NE_{bulk})}{2A} \quad [1]$$

where E_{slab} is the total energy the slab, E_{bulk} is the energy of a unit cell in the bulk of the film, N is the number of formula units within the slab, and A is the area of the surface. A slab is given by a finite number of layers of the material system that are fully periodic in x and y, and isolated from a periodic image in the z direction by a vacuum gap. E_{slab} and E_{bulk} were computed with periodic DFT using Quantum Espresso [28,29]. Pseudopotentials were given by the projector-augmented wave (PAW) method and used with the Perdew–Burke–Ernzerhof functional in the generalized gradient approximation. The kinetic energy cutoff for the wavefunction was set to 80 Ry, and a corresponding energy cutoff for the charge density was set to 800 Ry. A Monkhorst–Pack *k*-point grids of 4 × 4 × 4 and 4 × 4 × 1 were chosen for the Brillouin zone sampling of the bulk and the slab calculations, respectively. The super-cell for the bulk calculation consisted of a single unit cell. Variable cell optimization was performed on each bulk unit cell prior to the surface construction. Each super-cell for the surface calculations was constructed with a 30 Å thick slab and 15 Å vacuum gap. A geometry optimization with a fixed cell volume and shape was performed for each slab. All slabs were constructed with a complete number of perovskite formula units, resulting in two different terminations for the bottom and top surfaces. The surface energy for each termination was computed by freezing one of the surfaces in accordance with the procedure described previously [30] . One surface layer of the inorganic substructure composed of 1 Pb and 3 Br atoms was frozen in each slab, while the nuclei of the opposing surface was allowed to relax freely. All cations were set to rotate freely to account for the presence of the variety of cation orientations in the structure and its mobile nature. Due to the asymmetry introduced by the cation structure to the unit cell, cation orientation relative to the inorganic lattice and the surface was shown to break the degeneracy within a single family of plains [30]. In this study, we use the lowest energy surfaces as representative structures of the {100} and {110} families of planes. The chosen

cation orientations also agree with the structures reported in the literature [30,31]. The converged geometries for each surface calculation are provided in the supporting information (SI).

Characterization

SAXS: The SAXS measurements were performed on lead bromide solutions using the HZB ASAXS instrument [32] installed at the four-crystal monochromator beamline (FCM) of the Physikalisch-Technische Bundesanstalt (PTB) [33], and operated at the BESSYII synchrotron of Helmholtz-Zentrum Berlin für Materialien und Energie (HZB). The solutions were measured in transmission in flat rectangle shaped capillaries of 0.1 mm thickness under vacuum conditions using monochromatic X-rays of 10 keV. Data were collected three times for each sample with 600 s illumination per image. The images did not show any notable differences, implying that the solutions were stable under the chosen conditions. The 2D scattering patterns were azimuthally integrated and corrected for instrumental background and contributions of the sample holder through the BerSAS software [34].

GIWAXS: The GIWAXS measurements were performed at the beamline for Complex Materials Scattering (11-BM), at Brookhaven National Laboratory. The perovskite films for GIWAXS characterization were deposited on ITO/glass. An X-ray beam (13.5 keV, λ = 0.918 Å) with a footprint of 0.2 mm (height) × 0.05 mm (width) was irradiated on samples in vacuum (~10^{-5} torr) for 10 s with an incidence angle of 0.5°. Beam divergence was 1 mrad and energy resolution 0.7%. The data were analyzed using the SciAnalysis package provided by the beamline.

Photovoltaic performance: The current density–voltage (*J–V*) characteristics of the solar cells were measured using a LITOS LITE setup (Fluxim, Switzerland), equipped with a Wavelabs Sinus-70 AAA solar simulator with standard AM1.5 G illumination at room temperature and ambient air. The *J–V* curves were obtained in the range from 1.4 to −0.5 V with a scan speed of

50 mV·s^{-1} from both reverse and forward scan directions. The active area of the device was 0.128 cm^2, and a black metal mask with an aperture area of 0.0625 cm^2 was used to define the illuminated area.

Impedance spectroscopy (IS): IS was carried out in PAIOS hardware (Fluxim, Switzerland) on complete solar cells at room temperature under one sun illumination and in ambient air. The measurements were performed at different offset voltages from 0 V to the open circuit in 5 steps. The sweep frequency was from 10 MHz to 0.1 Hz, with an amplitude of 10.0 mV. Z-view software was employed to analyze the results and fit the data to the equivalent circuit.

3. Results and discussion

Early stages of crystallization

To analyze the perovskite precursor solutions, we measured SAXS of MABr-$PbBr_2$ and FABr-$PbBr_2$ precursors in DMF and DMSO (1 M). SAXS is a technique widely used to analyze the structure of nanoparticles in solution and their colloidal properties, and reveals information about sizes, distributions, and the interaction of these particles [20,35]. Flatken et. al introduced SAXS as a technique to reveal the colloidal nature of lead halide perovskites [20]. Moreover, SAXS allows for the analysis of high concentration solutions in comparison to other techniques such as dynamic light scattering (DLS) and UV-Vis spectroscopy, that necessitate lower concentrations [19,20,36]. **Figure 1** shows our SAXS results and interpretation. In **Figure 1A**, DMF presents clear and strong scattering peaks. In SAXS patterns, the scattering intensity indicates the presence of particles in solution. In addition, the scattering peak maximum results from particle interactions in solution [20]. This strong particle interaction indicates a quasi-crystalline prearrangement of particles in the early stages of crystallization [20,37]. The maximum peak position at q_{max} reveals the mean d spacing from Bragg's law $d = q_{max}/2\pi$. The d spacing is the distance between the mass centers of interacting colloidal particles. From Figure 1A, we calculate the q_{max} from a Lorentzian fitting and the d-

spacing (fitting in Figure S1). For both A-site cations in DMF there is colloidal particle interaction in solution. The calculated interparticle distance for both FA and MA particles is around 1.85 nm. Flatken et al. have shown a similar SAXS peak when preparing different lead iodide perovskites such as $MAPbI_3$ and $FAPbI_3$ in a mixture of DMF and DMSO [20,24]. However, the pure DMSO precursor solution showed no clear scattering peak (**Figure 1A**). In comparison to DMF, DMSO prevents the A-Pb-Br interaction as DMSO coordinates and binds stronger to the precursor salts. This suggests that there is no colloidal particle interaction. In contrast, in DMF, a solvent with weaker coordination, the colloidal particles interact with each other and form clusters [16]. This is in agreement with the previous work by Ray et al. which showed that due to the strong coordination of DMSO, the particles in solution do not interact with each other, remaining isolated [21]. This work also showed that DMSO forms colloidal particles one order of magnitude smaller than in DMF [21]. The schematic in **Figure 1B** shows the hypothesized differences in particle interaction for DMF and DMSO. The shape and composition of these particles are unknown, but we speculate, based on the work of Ray et al. [21] and Flatken et al. [24], that there are bromo-plumbate octahedra, the result of the interaction between A- Pb- Br in solution. We observe that in the bromide precursor solution, like in iodide perovskites [14,16], the colloidal particle interactions in solution are fully dependent on the solvent and the A-site does not show to play a role in the colloidal interactions.

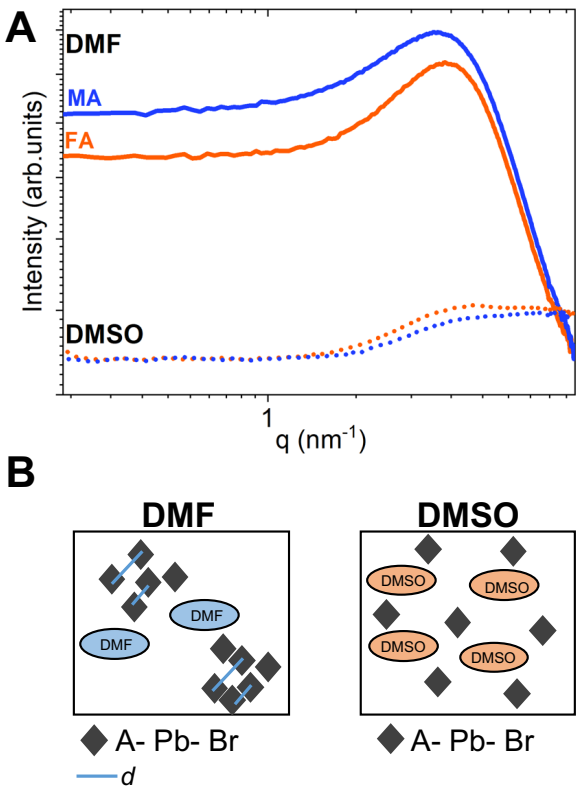

Figure 1. Particle interactions in the precursor solution. **A)** SAXS data for the four studied systems $MAPbBr_3$ in DMF or DMSO, and $FAPbBr_3$ in DMF or DMSO. **B)** Schematic of the particle interaction in DMF and DMSO interpreted from SAXS data, A is MA or FA, and *d* is the interparticle distance.

Preferred crystallographic orientation

We performed GIWAXS measurements on thin films prepared with DMF and DMSO to examine the effect of different cluster formation arising from the different solvents on the orientation of the thin films. Synchrotron-based GIWAXS has been widely used to analyze the crystallographic orientation and the structure of the lead halide perovskites in solar cells [26,38]. First, we study the effect of the solvent of the precursor solution on the crystal phases and crystallographic orientation by comparing the deposition of $FAPbBr_3$ and $MAPbBr_3$ in DMF, DMF: DMSO (4:1 volume), and DMSO. The 2D GIWAXS patterns were integrated to provide 1D diffraction patterns that are shown in Figure S2. For all the solvents, $MAPbBr_3$ [39] and $FAPbBr_3$ [40,41] display diffraction peaks corresponding to a cubic symmetry $Pm\bar{3}m$. To identify crystallographic orientations, we analyzed

the Debye-Scherrer rings from the GIWAXS patterns in **Figure 2**. **Figure 2A** shows the 2D GIWAXS for $MAPbBr_3$. As we change the solvent from DMF to DMSO, we see a clear evolution of the crystallographic orientation. For DMF, we observe a complete Debye-Scherrer ring of the (100) plane at $q \sim 1.06 \pm 0.06$ Å^{-1}, evidence of random orientation as the crystallographic domains scatter X-rays in all angles. The complete ring sharpens into an arc when adding one-fourth of the volume of DMSO, showing a preferred orientation of the crystallographic domains. For pure DMSO, the arc of the (100) plane sharpens further into a high-intensity Bragg spot, showing that the scattering of all crystallographic domains is in a single preferred orientation, an indication of high degree of preferred orientation. **Figure 2B** shows the 2D GIWAXS for $FAPbBr_3$, where the evolution and degree of orientation differ. For DMF and DMF: DMSO, $FAPbBr_3$ shows a uniform intensity in all the rings, suggesting the film has no preferred orientation. For pure DMSO, the ring of the (100) plane sharpens into an arc of high intensity at $q_r = 0$, increasing the degree of preferred crystallographic orientation from random to preferentially oriented crystallographic domains.

To further analyze and quantify crystallographic orientation, we integrated the azimuthal profile (χ) of the Debye-Scherrer rings of the first two peaks corresponding to the (100) plane at $q_r \sim 1.06 \pm 0.06$ Å^{-1}, and the (110) plane at $q_r \sim 1.4 \pm 0.06$ Å^{-1}. The peak of the azimuthal profile provides information about the direction of the preferred orientation of the planes. Since the grazing-incidence measurements give rise to a missing wedge near the q_z axis due to the curvature of the Ewald sphere, it is important to analyze the orientation of two planes. We studied the (100) and (110) planes, where the (110) plane complements the quantitative description about orientation. The (100) and (110) Debye-Scherrer rings are integrated from χ = -80° to 80°, where $\chi = 0°$ is set at $q_r = 0$ (out-of-plane) and $\chi = 90°$ at q_z=0 (in-plane). For $MAPbBr_3$, we integrated the azimuthal profile of the Debye-Scherrer rings from **Figure 2A** into **Figure 2C**, and for

$FAPbBr_3$, the azimuthal profiles are integrated from **Figure 2B** into **Figure 2D**. To understand the dispersion in orientation of the crystallographic domains, we fit the azimuthal profile peaks into a Pseudo-Voigt or Gaussian function from which we obtain the full width to half maximum (FWHM) and other statistical parameters shown in **Table S1**. The azimuthal profile for $MAPbBr_3$ in **Figure 2C** shows a peak at 0° of the (100) plane, evidence that these planes are oriented parallel to the substrate. In addition, the azimuthal profile peak of the (110) plane is around 45°, which is consistent with the (100) plane being oriented parallel to the substrate (explanation in Figure S3). We also observe that the choice of solvent changes the FWHM of the fitted azimuthal peak, as expected from the evolution in the degree of orientation seen in the 2D GIWAXS patterns in **Figure 2A**. For DMF, the (100) peak is broader, and the fitting has a larger error and low R^2 (Table S1). When DMSO is added (DMF: DMSO and pure DMSO), the azimuthal peaks sharpen, and the raw data fits nicely into the Pseudo Voigt function with a high R^2 (Table S1). The sharp azimuthal profile peaks indicate a high degree of preferred orientation of the (100) plane parallel to the substrate. In addition, the $MAPbBr_3$ with DMSO has the lowest FWHM, hence the higher degree of preferred orientation.

In **Figure 2D**, we observe the azimuthal profile peaks for $FAPbBr_3$. Compared to $MAPbBr_3$, the $FAPbBr_3$ peaks are all broader and have a higher FWHM, showing a lower degree of preferred orientation. For DMF, the crystallographic domains show dispersion in the integrated data, suggesting low degree of preferred orientation. The fitted Gaussian peak for DMF shows a very low R^2 and a large error in Table S1. The poor fitting for $FAPbBr_3$-DMF is evidence of random orientation. As we added DMSO to the precursor solution, we observed a better fit of the (100) azimuthal peak at 0°, showing that the crystallographic domains have an orientation of the (100) parallel to the substrate. However, the (110) azimuthal profile in $FAPbBr_3$-DMF: DMSO

shows three broad peaks at around ± 45° and 0°, which indicates a low degree and high dispersion in the orientation. With pure DMSO, the (100) azimuthal peak sharpens, the (110) azimuthal profile shows two bread peaks at ± 45° and the raw data fits better, with a higher R^2 and lower error in **Table S1** suggesting that pure DMSO shows some degree of preferred orientation. These results were corroborated by Bragg Brentano XRD to complement the missing wedge from GIWAXS (Figure S4).

The SAXS results discussed in the previous section suggest that there are interactions between the bromo-plumbate octahedra colloidal particles in DMF, which causes the possible formation of agglomerates in solution. We speculate that these colloidal aggregates could form dispersed and agglomerated nuclei in the crystallization process. This could lead to the random orientation observed in DMF from the GIWAXS measurements, as shown in the schematic of Figure S5. The higher degree of random orientation in DMF is observed regardless of cation type, indicative of this solvent dominated phenomena. However, to further understand the origins of preferred crystallographic orientation in lead bromide perovskites we now discuss MA and FA in pure DMSO; in DMSO there no longer are colloidal interactions. Instead, the octahedra particles and nuclei are isolated and the crystallization is slowed down. Moreover, from SAXS, we also learned that there were no differences between MA and FA in solution. However, the crystallized films in pure DMSO still show differences in orientation. For this reason, other underlying forces and mechanisms must lead to differences in orientation for the different A-site cations in lead bromide perovskites. Regardless of the solvent, we observe a clear difference in crystallographic orientation when we compare $MAPbBr_3$ and $FAPbBr_3$. The FWHM of the (100) azimuthal peak shown in **Figure 2E** quantifies the dispersion of orientation of the crystallographic domains. $MAPbBr_3$ films deposited from a pure DMSO precursor solution show the lowest FWHM,

evidence of the highest degree of preferred orientation. In contrast, $FAPbBr_3$ shows a higher FWHM, decreasing the degree of preferred orientation.

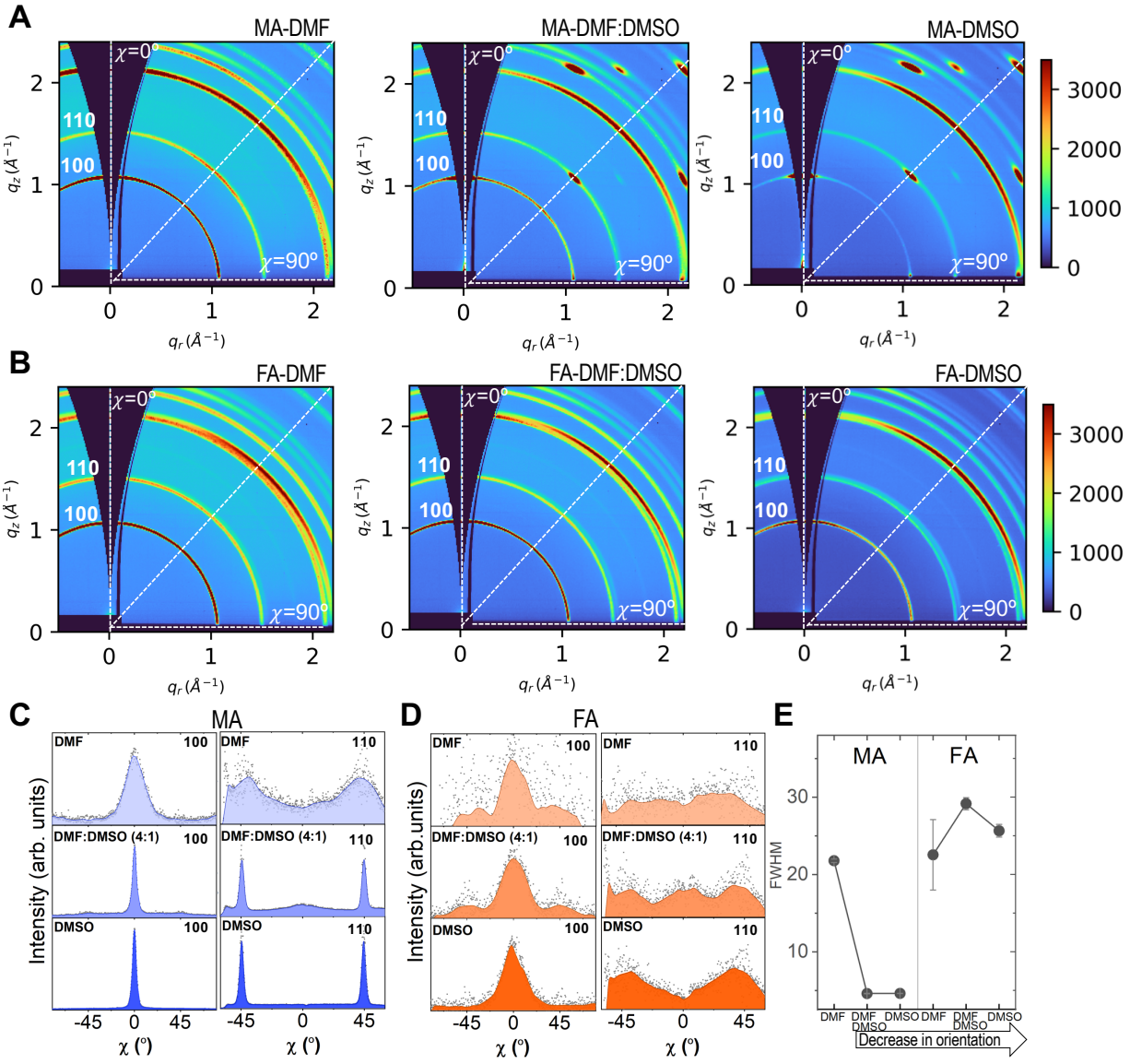

Figure 2. Interplay of solvent and A-site cation in the crystallographic orientation of lead bromide films studied by GIWAXS**. A,B)** 2D GIWAXS patterns in DMF, DMF:DMSO (4:1 volume), and DMSO for **A)** $MAPbBr_3$ and **B)** $FAPbBr_3$. **C,D)** Azimuthal integration profiles of the main Debye-Scherrer rings (100 and 110) as a function of the χ angle from GIWAXS for three solvent systems for **C)** $MAPbBr_3$ and **D)** $FAPbBr_3$. **E)** FWHM and error bar of the azimuthal peak for $MAPbBr_3$ and $FAPbBr_3$ as a function of the solvent.

Mechanisms for preferred orientation

We used periodic DFT to calculate the relative surface energies for $MAPbBr_3$ and $FAPbBr_3$ to help explain the difference in crystallographic orientation observed in the GIWAXS measurements arising from the difference in A-site cation. The calculated surface energies for a representative surface from the {100} and {110} family of planes are presented in **Figure 3A**. We considered both $PbBr_2$ and FABr/MABr termination, but we observed that the termination only leads to a qualitatively negligible variation in the surface energy regardless of A-site cation and surface plane. Therefore, the following qualitative conclusions are discussed regardless of this distinction.

Figure 3A shows that the (100) terminated slab is energetically more stable in comparison to the (110) terminated slab for $MAPbBr_3$, in agreement with previous calculations. In comparison, the (100) and (110) $FAPbBr_3$ have almost equivalent surface energies. The energy differences between the (110) and (100) surfaces for both cations are presented in **Figure 3B**. The large energy difference for MA compared to FA agrees with and helps explain the experimentally observed difference in crystallographic orientation. For MA, the (100) surface is energetically more stable and will therefore be the dominant surface that is formed. For FA, the relative degeneracy between the (100) and (110) surfaces imply no thermodynamic driving force to form one surface over the other. Therefore, both surfaces can be easily formed leading to a higher degree of orientational disorder. The relative difference in surface energies between $MAPbBr_3$ and $FAPbBr_3$ surface can be understood by examining the orientation of the A-site cation in the final surface structures (**Figure 3C**). In all cases, the organic A-site cation adopts a planar configuration with respect to the surface to minimize the energetic penalty of forming the surface. The difference is that in $MAPbBr_3$, the orientation of the A-site cation in the bulk already corresponds to a planar configuration; $MAPbBr_3$ only exhibits a minor geometric reorganization for both the (100) and (110) surfaces in comparison to the bulk structure associated with a rotation along the C-N bond

for the MA cation. Similarly, the FA cation is already planar in the (100) surface and therefore does not reorient significantly. However, the bulk configuration does not correspond to a planar configuration for the FA (110) surface. Therefore, the A-site cation can significantly reorient, which leads to an energetic stabilization of the (110) surface and results in the relative energy degeneracy between the (100) and (110) surfaces. This planar configuration of the FA cation has been previously observed in the context of $FAPbI_3$ [42]. While this analysis does not account for the kinetics of surface formation, the presence of two competing surface orientations in $FAPbBr_3$ provides thermodynamic insight into the increased disorder observed in the GIWAXS measurements **(Figure 3D)**.

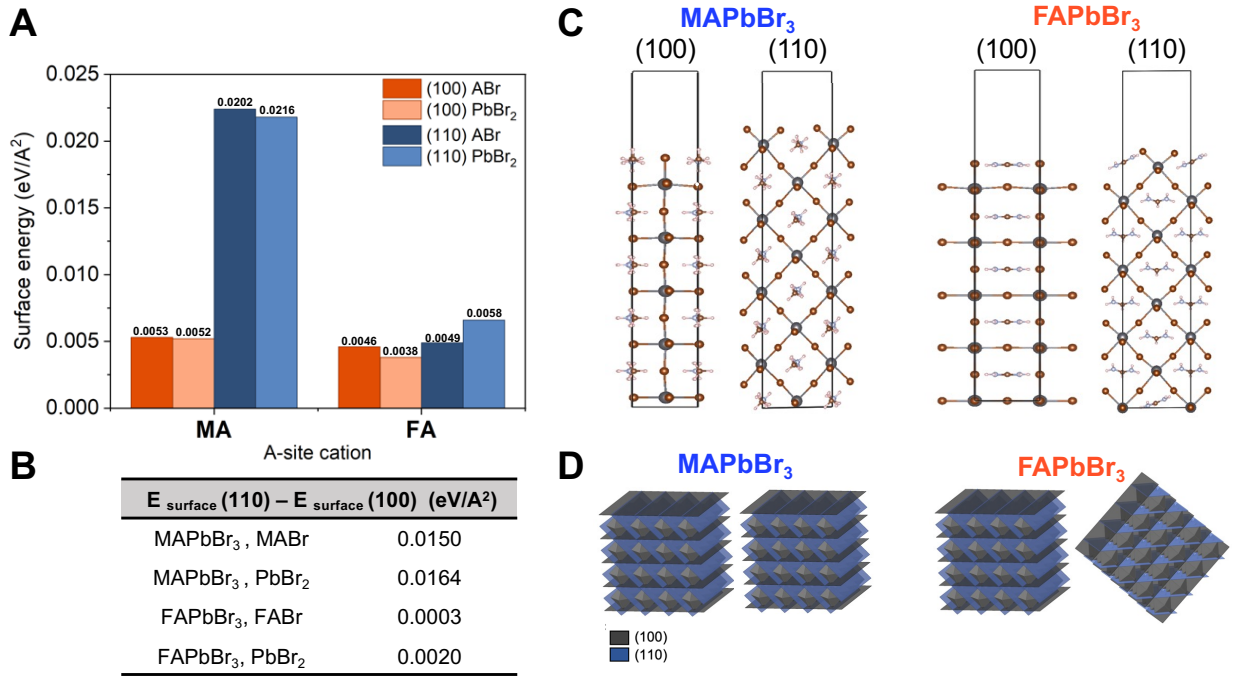

$E_{surface}$ (110) – $E_{surface}$ (100) (eV/A²)	
$MAPbBr_3$, MABr	0.0150
$MAPbBr_3$, $PbBr_2$	0.0164
$FAPbBr_3$, FABr	0.0003
$FAPbBr_3$, $PbBr_2$	0.0020

Figure 3. Results of the DFT calculation for the representative (100) and (110) surfaces of $MAPbBr_3$ and $FAPbBr_3$. **A**) Surface energy of the analyzed structures computed for surfaces with $PbBr_2$ or FABr/MABr termination. **B**) Energy difference between the corresponding (110) and (100) surfaces. **C**) Representative final structures of the FABr/MABr terminated calculation for $MAPbBr_3$ and $FAPbBr_3$. The inorganic lattice of the bottom surface that demonstrates the $PbBr_2$ phase was frozen throughout the calculation. **D**) Pictorial representation of the increased surface disorder due to the presence of two competing surfaces in $FAPbBr_3$.

Solar cell performance and ionic movement

Having understood the effect of the A-site cation on preferred crystallographic orientation, we studied these effects on the electric response in perovskite solar cells. Lead bromide perovskite solar cells exhibit significantly lower efficiency compared to their iodine counterparts due to their wider bandgap and unoptimized contacts. However, their large bandgap expands the scope of application into multijunction solar cells or other optoelectronic applications. We fabricated solar cells with the n-i-p architecture shown in **Figure 4A**, containing fluorine-doped tin oxide/ compact-TiO_2/ mesoporous-TiO_2/lead bromide perovskite $APbBr_3$/spiro-OMeTAD (2,2',7,7'-tetrakis(N,N-di-p-methozyphenyl-amine)9,9'-spirobifluorene)/Au. We measured the *J-V* characteristics of the solar cells under simulated solar illumination (AM 1.5 G, 100 mW/cm^2) to calculate the figures of merit of the solar cells. We measured the open circuit voltage, short circuit current, fill factor, and stabilized power conversion efficiency (PCE) from the maximum power point tracking (PCE_{MPPT}). The statistical distribution of the open circuit voltage is shown in **Figure 4B**. The optical bandgap (Figure S6) dominates the trends in the open circuit voltage. A larger bandgap for MA relative to FA increases the open circuit voltage and decreases the short circuit current (Figure S7). Given the differences in the bandgap, we cannot attribute the differences in charge carrier transport solely to crystallographic orientation. However, based on previous studies, a better charge carrier transport is expected for an oriented polycrystalline thin film [1,3]. The other figures of merit of the solar cells, fill factor, and PCE from the reverse scan are in the SI (Figure S7).

Beyond the effect of crystallographic orientation on charge carrier transport in perovskite solar cells, some studies have shown that orientation can influence the pathway of ionic movement. It has been shown that the halide and Pb ions can move along the (110) plane [2]. Therefore, we

analyze the hysteresis of the *J-V* curve to investigate how crystallographic orientation influences ion migration. Hysteresis of the *J-V* curve in lead halide perovskite solar cells has been attributed to ion migration [43–45]. Therefore, we calculated the absolute hysteresis index from the PCE to study the effects of ionic movement by comparing the difference between the forward scan (FS) and reverse scan (RS) of the PCE as follows [46]:

$$\text{Hysteresis } \% = \frac{|PCE_{RS} - PCE_{FS}|}{\text{PCE}_{\text{RS}}} \quad [2]$$

The devices made with $FAPbBr_3$ perovskites show a lower hysteresis than those made with $MAPbBr_3$. This hysteresis behavior associated with ion migration that is dependent on lead halide perovskite composition is in line with the previous reports [43,45,47]. In $MAPbBr_3$, the defect activation energy barrier for ion movement has been calculated to be lower than that of $FAPbBr_3$, giving rise to more ionic movement, and explaining the larger hysteresis behavior for $MAPbBr_3$. In addition, the hydrogen bond between the organic A-site cation and the bromine is stronger for FA than MA, limiting the motion of the cation in the case of $FAPbBr_3$ [47]. This could be an additional explanation for the increase in hysteresis in $MAPbBr_3$ solar cells.

To further understand the role of A-site cation on ionic motion in these materials, we measured impedance spectroscopy under different biases. The resulting Nyquist plots reproduce the characteristic patterns of lead halide perovskite solar cells [48] (see representative spectra in Figure S8). The Nyquist plots were fitted to an equivalent circuit reported elsewhere (illustrated in **Figure 4C**) [49]. This circuit includes a resistor (R_{rec+tr}) that couples both the recombination and transport resistances due to the low chemical capacitance of perovskite solar cells and a low-frequency branch with a capacitor (C_{dr}) and resistor (R_{dr}), both related to the ionic nature of the lead halide perovskites. In **Figure 4D**, R_{rec+tr} displays negligible variations between $MAPbBr_3$ and $FAPbBr_3$ under lower bias values.

High capacitance values at low-frequency regimes have been a fingerprint of lead halide perovskite solar cells [49]. The origin of this low-frequency capacitance is typically attributed to the mixed ionic-electronic nature of these materials [48,50]. In the equivalent circuit employed to analyze the results, this capacitance is modeled by a constant phase element C_{dr} to account for dispersive phenomena, yet with exponent values close to 1. The C_{dr} can be interpreted as an indication of increased ionic density or as higher ionic diffusion [51]. Therefore, a comparative analysis of the C_{dr} is used to understand the ionic differences between $MAPbBr_3$ and $FAPbBr_3$, as observed in **Figure 4D**. FA has a slightly lower C_{dr} than MA. The slight reduction of C_{dr} can be interpreted as an indication of increased ionic diffusion or higher ionic density in $FAPbBr_3$. To decouple the effects between ionic density and ionic diffusion, we examined the low-frequency part of the spectrum R_{dr}. The increase of R_{dr} for $FAPbBr_3$ compared to $MAPbBr_3$ confirms the higher ionic density of the latter. These variations are in line with the increase of the absolute *J-V* hysteresis in $MAPbBr_3$ solar cells (**Figure 4B**). These experimental results align with published computational results [47] in which bromide vacancies and interstitials had much lower formation energies and higher densities in $MAPbBr_3$ than for $FAPbBr_3$, where the FA cation suppressed ion diffusion.

Analyzing the effect of preferred crystallographic orientation on the ionic effects, we observe that the highly preferentially oriented $MAPbBr_3$ has the highest ionic density compared to the randomly oriented $FAPbBr_3$. We suggest that ionic effects could be affected by the crystallographic orientation in lead bromide perovskites. Previous studies have shown the effects of in-plane crystallographic orientation of lead halide perovskites, where it has been observed that preferred orientation leads to a higher movement of ions. Fassl et al. studied the effect of in-plane crystallographic orientation on ionic transport rate from simulations and experimental work [52]. They found that the relative orientation of the crystals affects ionic migration in polycrystalline

films; aligned crystals had uniform ion transport, while randomly oriented crystals had varying rates of ionic transport. Further, Eames et al. showed that in perovskite films with vacancy defects, ions have favorable crystallographic planes to move [53]. The halide migrates along the octahedron edge between halide sites [53]. Given that mobile ions can move in the <110> family of directions, Flannery et al. [2] observed that ionic movement through the absorber layer is higher if the crystals in a mixed-halide lead halide perovskite film were highly oriented in the (110) plane. While an effect of orientation on charge transport cannot be excluded, we show that increased preferred orientation along the (100) plane does not contribute to an improved ion diffusion. Differences in the ionic contribution are ascribed to an increased ionic density in the highly ordered $MAPbBr_3$ perovskite.

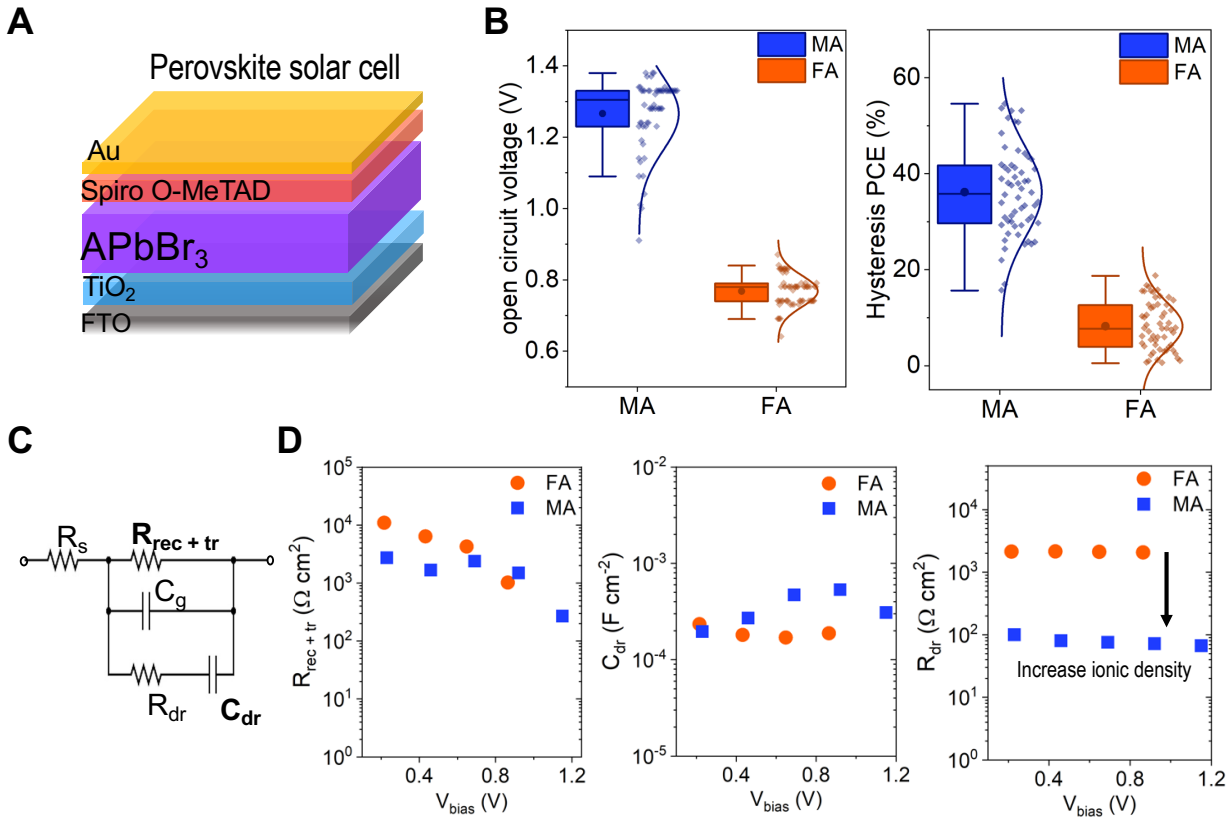

Figure 4. Electrical properties of solar cell. **A)** Perovskite solar cell architecture where A in $APbBr_3$ is MA or FA, **B)** Box plots of the solar cell characterization from *J-V* curve **i)** open circuit

voltage, and **ii)** absolute hysteresis index of the power conversion efficiency (PCE). **C)** Impedance spectroscopy measurements for $MAPbBr_3$ and $FAPbBr_3$ **i)** Equivalent circuit used for the analysis of the impedance spectra, i**i)** Recombination and transport resistance for different applied biases, and **iii)** low-frequency capacitance for different applied biases.

4. Conclusions

We studied the effect of the solvent and organic A-site cation on the crystallographic orientation in lead bromide thin films. We showed that there is an interplay between the type of solvent and A-site cation that determines the preferred crystallographic orientation in bromine-based perovskites. Polycrystalline thin films prepared from solutions in DMF solvents exhibit less orientation, whereas films prepared from solutions in DMSO exhibit higher degree of preferred orientation for both FA and MA. Regardless of the solvent, $MAPbBr_3$ showed a higher degree of preferred orientation compared to $FAPbBr_3$. Theoretical calculations showed that thermodynamically, $MAPbBr_3$ is energetically favored to grow along the (100) plane, while in $FAPbBr_3$ the (100) and (110) surfaces are nearly degenerate in energy, and both are equally favored for growth. In addition, we observed that there are larger ionic movement effects in the highly oriented $MAPbBr_3$ solar cells. The *J-V* hysteresis of the solar cells, and impedance spectroscopy results, indicate higher ionic density effects in $MAPbBr_3$. This work provides new insights on the role of both solvent and A-site cation on the crystallization of thin films.

5. Associated content

Supporting Information. The supporting information is available free of charge at: https://pbs.acs.org... The supplementary document includes complete experimental section with materials and methods; Iodide-based results; peak assignment for the $Cs_{0.17}FA_{0.83}PbBr_3$ sample after humidity exposure; details on the azimuthal integration from GIWAXS; further SEM images and the complete optical properties values of all studied films; Survey spectra and complete information on XPS; Details about the TRMC setup and perovskite lifetimes; Impedance spectroscopy complete data.

6. Author information

Corresponding Authors: Juan-Pablo Correa-Baena, Joshua S. Kretchmer

Author contributions: J.H formulated the project and wrote the manuscript. Fabricated thin films and solar cells, performed, and analyzed the GIWAXS experiments, performed and analyzed DLS, and performed IS measurements on solar cells. Y.A helped formulating the project, fabricated thin films and solar cells, characterized SEM, UV-Vis, PL, and general data analysis. D.Y helped in the analysis of the data, performed the computational work, and analyzed it. R.L performed GIWAXS data collection and analysis at BNL. A.H performed the SAXS experiments and the data reduction. C.A.R.P assisted in the analysis and writing of the whole manuscript. J.B performed SAXS data collection and analysis at BESSY. S.S Oversaw and analyzed the SAXS data and revised all the manuscript. P.B analyzed all the IS data and interpretation. J.S.K supervised the computational work and participated in the whole data analysis of the manuscript. J.P.C.B supervised the entire work, helped in analysis, manuscript writing, and revision. All the authors have read, corrected, and agree with the manuscript.

Notes: The authors declare no competing financial interest.

7. Acknowledgement

This work was performed in part of the Georgia Tech Institute for Electronics and Nanotechnology, a member of the National Nanotechnology Coordinated Infrastructure (NNCI), which is supported by the National Science Foundation (Grant ECCS-1542174). J.H. acknowledges the Department of Education Graduate Assistance in Areas of National Need (GAANN) program at Georgia Institute of Technology (Award #P200A180075), and the Graduate Education for Minorities (GEM) fellowship for career funding. Y.A. thanks the China Scholarship Council (CSC) for financial support from fellowship No. 201906250003, and financial support from the National Science Foundation of China (No. 21676188). This research used the CMS 11-BM beamline of the National Synchrotron Light Source II, a U.S Department of Energy (DOE) Office Science User Facility operated for the DOE office of Science by Brookhaven National Laboratory under Contract DE-SC0012704. J.H and Y.A also thank all the members of the Energy Materials Laboratory at Georgia Tech for their help and discussions about the project. J.H, J.B, A.H and S.S would like to thank Ana Palacios-Saura, Niyaz Huseyn-Zada and Dr. Uwe Keiderling for assistance with the SAXS measurements. J.B, A.H, and S.S thank the PTB (the German national metrology institute) for the ability to use the FCM beamline at BESSYII of Helmholtz-Zentrum Berlin to carry out SAXS measurements, especially Dieter Skroblin and Christian Gollwitzer for the experimental support.

8. References

(1) Hidalgo, J.; Perini, C. A. R.; Castro-Mendez, A.-F.; Jones, D.; Köbler, H.; Lai, B.; Li, R.; Sun, S.; Abate, A.; Correa-Baena, J.-P. Moisture-Induced Crystallographic Reorientations and Effects on Charge Carrier Extraction in Metal Halide Perovskite Solar Cells. *ACS Energy Lett.* **2020**, *5* (11), 3526–3534. https://doi.org/10.1021/acsenergylett.0c01964.

(2) Flannery, L.; Ogle, J.; Powell, D.; Tassone, C.; Whittaker-Brooks, L. Voltage Bias Stress Effects in Metal Halide Perovskites Are Strongly Dependent on Morphology and Ion Migration Pathways. *J. Mater. Chem. A* **2020**, *8* (47), 25109–25119. https://doi.org/10.1039/D0TA10371C.

(3) Zheng, G.; Zhu, C.; Ma, J.; Zhang, X.; Tang, G.; Li, R.; Chen, Y.; Li, L.; Hu, J.; Hong, J.; Chen, Q.; Gao, X.; Zhou, H. Manipulation of Facet Orientation in Hybrid Perovskite Polycrystalline Films by Cation Cascade. *Nature Communications* **2018**, *9* (1), 1–11. https://doi.org/10.1038/s41467-018-05076-w.
(4) Rivnay, J.; Mannsfeld, S. C. B.; Miller, C. E.; Salleo, A.; Toney, M. F. Quantitative Determination of Organic Semiconductor Microstructure from the Molecular to Device Scale. *Chem. Rev.* **2012**, *112* (10), 5488–5519. https://doi.org/10.1021/cr3001109.
(5) Joseph Kline, R.; McGehee, M. D.; Toney, M. F. Highly Oriented Crystals at the Buried Interface in Polythiophene Thin-Film Transistors. *Nature Mater* **2006**, *5* (3), 222–228. https://doi.org/10.1038/nmat1590.
(6) Vasileiadou, E. S.; Hadar, I.; Kepenekian, M.; Even, J.; Tu, Q.; Malliakas, C. D.; Friedrich, D.; Spanopoulos, I.; Hoffman, J. M.; Dravid, V. P.; Kanatzidis, M. G. Shedding Light on the Stability and Structure–Property Relationships of Two-Dimensional Hybrid Lead Bromide Perovskites. *Chem. Mater.* **2021**, *33* (13), 5085–5107. https://doi.org/10.1021/acs.chemmater.1c01129.
(7) Kulbak, M.; Gupta, S.; Kedem, N.; Levine, I.; Bendikov, T.; Hodes, G.; Cahen, D. Cesium Enhances Long-Term Stability of Lead Bromide Perovskite-Based Solar Cells. *J. Phys. Chem. Lett.* **2016**, *7* (1), 167–172. https://doi.org/10.1021/acs.jpclett.5b02597.
(8) Ijaz, P.; Imran, M.; Soares, M. M.; Tolentino, H. C. N.; Martín-García, B.; Giannini, C.; Moreels, I.; Manna, L.; Krahne, R. Composition-, Size-, and Surface Functionalization-Dependent Optical Properties of Lead Bromide Perovskite Nanocrystals. *J. Phys. Chem. Lett.* **2020**, *11* (6), 2079–2085. https://doi.org/10.1021/acs.jpclett.0c00266.
(9) Leyden, M. R.; Meng, L.; Jiang, Y.; Ono, L. K.; Qiu, L.; Juarez-Perez, E. J.; Qin, C.; Adachi, C.; Qi, Y. Methylammonium Lead Bromide Perovskite Light-Emitting Diodes by Chemical Vapor Deposition. *J. Phys. Chem. Lett.* **2017**, *8* (14), 3193–3198. https://doi.org/10.1021/acs.jpclett.7b01093.
(10) Gavranovic, S.; Pospisil, J.; Zmeskal, O.; Novak, V.; Vanysek, P.; Castkova, K.; Cihlar, J.; Weiter, M. Electrode Spacing as a Determinant of the Output Performance of Planar-Type Photodetectors Based on Methylammonium Lead Bromide Perovskite Single Crystals. *ACS Appl. Mater. Interfaces* **2022**, *14* (17), 20159–20167. https://doi.org/10.1021/acsami.1c24362.
(11) Hu, C.; Shivarudraiah, S. B.; Sung, H. H. Y.; Williams, I. D.; Halpert, J. E.; Yang, S. Discovery of a New Intermediate Enables One-Step Deposition of High-Quality Perovskite Films via Solvent Engineering. *Solar RRL* **2021**, *5* (4), 2000712. https://doi.org/10.1002/solr.202000712.
(12) Rezaee, E.; Zhang, W.; Silva, S. R. P. Solvent Engineering as a Vehicle for High Quality Thin Films of Perovskites and Their Device Fabrication. *Small* **2021**, *17* (25), 2008145. https://doi.org/10.1002/smll.202008145.
(13) Shargaieva, O.; Näsström, H.; Smith, J. A.; Többens, D.; Munir, R.; Unger, E. Hybrid Perovskite Crystallization from Binary Solvent Mixtures: Interplay of Evaporation Rate and Binding Strength of Solvents. *Mater. Adv.* **2020**, *1* (9), 3314–3321. https://doi.org/10.1039/D0MA00815J.
(14) Petrov, A. A.; Sokolova, I. P.; Belich, N. A.; Peters, G. S.; Dorovatovskii, P. V.; Zubavichus, Y. V.; Khrustalev, V. N.; Petrov, A. V.; Grätzel, M.; Goodilin, E. A.; Tarasov, A. B. Crystal

Structure of DMF-Intermediate Phases Uncovers the Link Between $CH_3NH_3PbI_3$ Morphology and Precursor Stoichiometry. *J. Phys. Chem. C* **2017**, *121* (38), 20739–20743. https://doi.org/10.1021/acs.jpcc.7b08468.

(15) Soe, C. M. M.; Nie, W.; Stoumpos, C. C.; Tsai, H.; Blancon, J.-C.; Liu, F.; Even, J.; Marks, T. J.; Mohite, A. D.; Kanatzidis, M. G. Understanding Film Formation Morphology and Orientation in High Member 2D Ruddlesden–Popper Perovskites for High-Efficiency Solar Cells. *Advanced Energy Materials* **2018**, *8* (1), 1700979. https://doi.org/10.1002/aenm.201700979.

(16) Hamill, J. C.; Schwartz, J.; Loo, Y.-L. Influence of Solvent Coordination on Hybrid Organic–Inorganic Perovskite Formation. *ACS Energy Lett.* **2018**, *3* (1), 92–97. https://doi.org/10.1021/acsenergylett.7b01057.

(17) Petrov, A. A.; Ordinartsev, A. A.; Fateev, S. A.; Goodilin, E. A.; Tarasov, A. B. Solubility of Hybrid Halide Perovskites in DMF and DMSO. *Molecules* **2021**, *26* (24), 7541. https://doi.org/10.3390/molecules26247541.

(18) Petrov, A. A.; Fateev, S. A.; Khrustalev, V. N.; Li, Y.; Dorovatovskii, P. V.; Zubavichus, Y. V.; Goodilin, E. A.; Tarasov, A. B. Formamidinium Haloplumbate Intermediates: The Missing Link in a Chain of Hybrid Perovskites Crystallization. *Chem. Mater.* **2020**, *32* (18), 7739–7745. https://doi.org/10.1021/acs.chemmater.0c02156.

(19) Dutta, N. S.; Noel, N. K.; Arnold, C. B. Crystalline Nature of Colloids in Methylammonium Lead Halide Perovskite Precursor Inks Revealed by Cryo-Electron Microscopy. *J. Phys. Chem. Lett.* **2020**, *11* (15), 5980–5986. https://doi.org/10.1021/acs.jpclett.0c01975.

(20) Flatken, M. A.; Hoell, A.; Wendt, R.; Härk, E.; Dallmann, A.; Prause, A.; Pascual, J.; Unger, E.; Abate, A. Small-Angle Scattering to Reveal the Colloidal Nature of Halide Perovskite Precursor Solutions. *J. Mater. Chem. A* **2021**, *9* (23), 13477–13482. https://doi.org/10.1039/D1TA01468D.

(21) Ray, A.; Maggioni, D.; Baranov, D.; Dang, Z.; Prato, M.; Akkerman, Q. A.; Goldoni, L.; Caneva, E.; Manna, L.; Abdelhady, A. L. Green-Emitting Powders of Zero-Dimensional Cs_4PbBr_6 : Delineating the Intricacies of the Synthesis and the Origin of Photoluminescence. *Chem. Mater.* **2019**, *31* (18), 7761–7769. https://doi.org/10.1021/acs.chemmater.9b02944.

(22) Bo Chen; Zhengshan J. Yu; Salman Manzoor; Shen Wang; William Weigand; Zhenhua Yu; Guang Yang; Zhenyi Ni; Zuezeng Dai; Zachary C. Holman; Jinsong Huang. Blade-Coated Perovskites on Textured Silicon for 26%-Efficient Monolithic Perovskite/Silicon Tandem Solar Cells | Elsevier Enhanced Reader. *Joule* **2020**, *4*, 850–864. https://doi.org/10.1016/j.joule.2020.01.008.

(23) Zhang, J.; Zhang, L.; Li, X.; Zhu, X.; Yu, J.; Fan, K. Binary Solvent Engineering for High-Performance Two-Dimensional Perovskite Solar Cells. *ACS Sustainable Chem. Eng.* **2019**, *7* (3), 3487–3495. https://doi.org/10.1021/acssuschemeng.8b05734.

(24) Flatken, M. A.; Radicchi, E.; Wendt, R.; Buzanich, A. G.; Härk, E.; Pascual, J.; Mathies, F.; Shargaieva, O.; Prause, A.; Dallmann, A.; De Angelis, F.; Hoell, A.; Abate, A. Role of the Alkali Metal Cation in the Early Stages of Crystallization of Halide Perovskites. *Chem. Mater.* **2022**, *34* (3), 1121–1131. https://doi.org/10.1021/acs.chemmater.1c03563.

(25) Keller, T.; Nickel, N. H.; Rappich, J. Competition of Iodide/Bromide Ions in the Formation of Methylammonium Lead Halide in Different Solvents. *J. Phys. Chem. C* **2022**, *126* (41), 17656–17662. https://doi.org/10.1021/acs.jpcc.2c03740.

(26) Steele, J. A.; Solano, E.; Jin, H.; Prakasam, V.; Braeckevelt, T.; Yuan, H.; Lin, Z.; de Kloe, R.; Wang, Q.; Rogge, S. M. J.; Van Speybroeck, V.; Chernyshov, D.; Hofkens, J.; Roeffaers, M. B. J. Texture Formation in Polycrystalline Thin Films of All-Inorganic Lead Halide Perovskite. *Advanced Materials* **2021**, *33* (13), 1–9. https://doi.org/10.1002/adma.202007224.

(27) An, Y.; Perini, C. A. R.; Hidalgo, J.; Castro-Méndez, A.-F.; Vagott, J. N.; Li, R.; Saidi, W. A.; Wang, S.; Li, X.; Correa-Baena, J.-P. Identifying High-Performance and Durable Methylammonium-Free Lead Halide Perovskites *via* High-Throughput Synthesis and Characterization. *Energy Environ. Sci.* **2021**, *14* (12), 6638–6654. https://doi.org/10.1039/D1EE02691G.

(28) Giannozzi, P.; Baroni, S.; Bonini, N.; Calandra, M.; Car, R.; Cavazzoni, C.; Ceresoli, D.; Chiarotti, G. L.; Cococcioni, M.; Dabo, I.; Dal Corso, A.; de Gironcoli, S.; Fabris, S.; Fratesi, G.; Gebauer, R.; Gerstmann, U.; Gougoussis, C.; Kokalj, A.; Lazzeri, M.; Martin-Samos, L.; Marzari, N.; Mauri, F.; Mazzarello, R.; Paolini, S.; Pasquarello, A.; Paulatto, L.; Sbraccia, C.; Scandolo, S.; Sclauzero, G.; Seitsonen, A. P.; Smogunov, A.; Umari, P.; Wentzcovitch, R. M. QUANTUM ESPRESSO: A Modular and Open-Source Software Project for Quantum Simulations of Materials. *J. Phys.: Condens. Matter* **2009**, *21* (39), 395502. https://doi.org/10.1088/0953-8984/21/39/395502.

(29) Giannozzi, P.; Andreussi, O.; Brumme, T.; Bunau, O.; Buongiorno Nardelli, M.; Calandra, M.; Car, R.; Cavazzoni, C.; Ceresoli, D.; Cococcioni, M.; Colonna, N.; Carnimeo, I.; Dal Corso, A.; de Gironcoli, S.; Delugas, P.; DiStasio, R. A.; Ferretti, A.; Floris, A.; Fratesi, G.; Fugallo, G.; Gebauer, R.; Gerstmann, U.; Giustino, F.; Gorni, T.; Jia, J.; Kawamura, M.; Ko, H.-Y.; Kokalj, A.; Küçükbenli, E.; Lazzeri, M.; Marsili, M.; Marzari, N.; Mauri, F.; Nguyen, N. L.; Nguyen, H.-V.; Otero-de-la-Roza, A.; Paulatto, L.; Poncé, S.; Rocca, D.; Sabatini, R.; Santra, B.; Schlipf, M.; Seitsonen, A. P.; Smogunov, A.; Timrov, I.; Thonhauser, T.; Umari, P.; Vast, N.; Wu, X.; Baroni, S. Advanced Capabilities for Materials Modelling with Quantum ESPRESSO. *J. Phys.: Condens. Matter* **2017**, *29* (46), 465901. https://doi.org/10.1088/1361-648X/aa8f79.

(30) Guo, Y.; Li, C.; Li, X.; Niu, Y.; Hou, S.; Wang, F. Effects of Rb Incorporation and Water Degradation on the Stability of the Cubic Formamidinium Lead Iodide Perovskite Surface: A First-Principles Study. *J. Phys. Chem. C* **2017**, *121* (23), 12711–12717. https://doi.org/10.1021/acs.jpcc.7b01390.

(31) Moon, J.; Kwon, S.; Alahbakhshi, M.; Lee, Y.; Cho, K.; Zakhidov, A.; Kim, M. J.; Gu, Q. Surface Energy-Driven Preferential Grain Growth of Metal Halide Perovskites: Effects of Nanoimprint Lithography Beyond Direct Patterning. *ACS Appl. Mater. Interfaces* **2021**, *13* (4), 5368–5378. https://doi.org/10.1021/acsami.0c17655.

(32) Hoell, A.; Zizak, I.; Mokrani, L. Einrichtung Zur Kleinwinkelstreumessung Zur Analyse Der Nanostruktur an Proben Mittels Röntgenstrahlung. DE102006029449B3, 2007.

(33) Krumrey, M.; Ulm, G. High-Accuracy Detector Calibration at the PTB Four-Crystal Monochromator Beamline. *Nuclear Instruments & Methods in Physics Research: Section A* **2001**, No. 467–468, 1175–1178. https://doi.org/DOI: 10.1016/S0168-9002(01)00598-8.

(34) Keiderling, U. The New "BerSANS-PC" Software for Reduction and Treatment of Small Angle Neutron Scattering Data. *Applied Physics A: Materials Science & Processing* **2002**, *74* (0), s1455–s1457. https://doi.org/10.1007/s003390201561.

(35) Feigin, L.A; Svergun, D.I. *Structure Analysis by Small-Angle X-Ray and Neutron Scattering*; Plenum Press, New York, 1987.

(36) Qin, F.; Wang, Z.; Wang, Z. L. Anomalous Growth and Coalescence Dynamics of Hybrid Perovskite Nanoparticles Observed by Liquid-Cell Transmission Electron Microscopy. *ACS Nano* **2016**, *10* (11), 9787–9793. https://doi.org/10.1021/acsnano.6b04234.
(37) Hao, X.; Chen, M.; Wang, L.; Cao, Z.; Li, Y.; Han, S.; Zhang, M.; Yu, K.; Zeng, J. *In Situ* SAXS Probing the Evolution of the Precursors and Onset of Nucleation of ZnSe Colloidal Semiconductor Quantum Dots. *Chem. Commun.* **2020**, *56* (13), 2031–2034. https://doi.org/10.1039/C9CC09274A.
(38) Ogle, J.; Powell, D.; Amerling, E.; Smilgies, D.-M.; Whittaker-Brooks, L. Quantifying Multiple Crystallite Orientations and Crystal Heterogeneities in Complex Thin Film Materials. *CrystEngComm* **2019**, *21* (38), 5707–5720. https://doi.org/10.1039/C9CE01010F.
(39) Wang, K.-H.; Li, L.-C.; Shellaiah, M.; Wen Sun, K. Structural and Photophysical Properties of Methylammonium Lead Tribromide (MAPbBr3) Single Crystals. *Sci Rep* **2017**, *7* (1), 13643. https://doi.org/10.1038/s41598-017-13571-1.
(40) Franz, A.; Többens, D. M.; Lehmann, F.; Kärgell, M.; Schorr, S. The Influence of Deuteration on the Crystal Structure of Hybrid Halide Perovskites: A Temperature-Dependent Neutron Diffraction Study of $FAPbBr_3$. *Acta Crystallogr B Struct Sci Cryst Eng Mater* **2020**, *76* (2), 267–274. https://doi.org/10.1107/S2052520620002620.
(41) Schueller, E. C.; Laurita, G.; Fabini, D. H.; Stoumpos, C. C.; Kanatzidis, M. G.; Seshadri, R. Crystal Structure Evolution and Notable Thermal Expansion in Hybrid Perovskites Formamidinium Tin Iodide and Formamidinium Lead Bromide. *Inorg. Chem.* **2018**, *57* (2), 695–701. https://doi.org/10.1021/acs.inorgchem.7b02576.
(42) Oner, S. M.; Sezen, E.; Yordanli, M. S.; Karakoc, E.; Deger, C.; Yavuz, I. Surface Defect Formation and Passivation in Formamidinium Lead Triiodide ($FAPbI_3$) Perovskite Solar Cell Absorbers. *J. Phys. Chem. Lett.* **2022**, *13* (1), 324–330. https://doi.org/10.1021/acs.jpclett.1c03645.
(43) Chen, B.; Yang, M.; Priya, S.; Zhu, K. Origin of J – V Hysteresis in Perovskite Solar Cells. *J. Phys. Chem. Lett.* **2016**, *7* (5), 905–917. https://doi.org/10.1021/acs.jpclett.6b00215.
(44) McGovern, L.; Koschany, I.; Grimaldi, G.; Muscarella, L. A.; Ehrler, B. Grain Size Influences Activation Energy and Migration Pathways in $MAPbBr_3$ Perovskite Solar Cells. *J. Phys. Chem. Lett.* **2021**, *12* (9), 2423–2428. https://doi.org/10.1021/acs.jpclett.1c00205.
(45) Liu, P.; Wang, W.; Liu, S.; Yang, H.; Shao, Z. Fundamental Understanding of Photocurrent Hysteresis in Perovskite Solar Cells. *Advanced Energy Materials* **2019**, *9* (13), 1803017. https://doi.org/10.1002/aenm.201803017.
(46) Zhu, X.; Du, M.; Feng, J.; Wang, H.; Xu, Z.; Wang, L.; Zuo, S.; Wang, C.; Wang, Z.; Zhang, C.; Ren, X.; Priya, S.; Yang, D.; Liu, S. (Frank). High-Efficiency Perovskite Solar Cells with Imidazolium-Based Ionic Liquid for Surface Passivation and Charge Transport. *Angewandte Chemie International Edition* **2021**, *60* (8), 4238–4244. https://doi.org/10.1002/anie.202010987.
(47) Oranskaia, A.; Yin, J.; Bakr, O. M.; Brédas, J.-L.; Mohammed, O. F. Halogen Migration in Hybrid Perovskites: The Organic Cation Matters. *J. Phys. Chem. Lett.* **2018**, *9* (18), 5474–5480. https://doi.org/10.1021/acs.jpclett.8b02522.
(48) Pitarch-Tena, D.; Ngo, T. T.; Vallés-Pelarda, M.; Pauporté, T.; Mora-Seró, I. Impedance Spectroscopy Measurements in Perovskite Solar Cells: Device Stability and Noise Reduction. *ACS Energy Lett.* **2018**, *3* (4), 1044–1048. https://doi.org/10.1021/acsenergylett.8b00465.

(49) *An Equivalent Circuit for Perovskite Solar Cell Bridging Sensitized to Thin Film Architectures | Elsevier Enhanced Reader*. https://doi.org/10.1016/j.joule.2019.07.014.
(50) Zarazua, I.; Bisquert, J.; Garcia-Belmonte, G. Light-Induced Space-Charge Accumulation Zone as Photovoltaic Mechanism in Perovskite Solar Cells. *J. Phys. Chem. Lett.* **2016**, *7* (3), 525–528. https://doi.org/10.1021/acs.jpclett.5b02810.
(51) Riquelme, A. J.; Valadez-Villalobos, K.; Boix, P. P.; Oskam, G.; Mora-Seró, I.; Anta, J. A. Understanding Equivalent Circuits in Perovskite Solar Cells. Insights from Drift-Diffusion Simulation. *Phys. Chem. Chem. Phys.* **2022**, *24* (26), 15657–15671. https://doi.org/10.1039/D2CP01338J.
(52) Fassl, P.; Ternes, S.; Lami, V.; Zakharko, Y.; Heimfarth, D.; Hopkinson, P. E.; Paulus, F.; Taylor, A. D.; Zaumseil, J.; Vaynzof, Y. Effect of Crystal Grain Orientation on the Rate of Ionic Transport in Perovskite Polycrystalline Thin Films. *ACS Appl. Mater. Interfaces* **2019**, *11* (2), 2490–2499. https://doi.org/10.1021/acsami.8b16460.
(53) Eames, C.; Frost, J. M.; Barnes, P. R. F.; O'Regan, B. C.; Walsh, A.; Islam, M. S. Ionic Transport in Hybrid Lead Iodide Perovskite Solar Cells. *Nature Communications* **2015**, *6* (May), 2–9. https://doi.org/10.1038/ncomms8497.